Pure & Appl. Chem., Vol. 57, No. 1, pp. 31–44, 1985.
Printed in Great Britain.

Some thermodynamic aspects of geochemistry

Harold C. Helgeson

Department of Geology and Geophysics, University of California, Berkeley, California 94720, USA

Abstract — Application of thermodynamics to the study of geologic systems permits prediction of equilibrium relations among minerals and aqueous species at pressures and temperatures to ~ 5 kb and ~ 1000°C. The predictions afford a frame of reference for interpreting phase relations in geologic systems and assessing thermodynamic constraints on reaction rates and interphase mass transfer in geochemical processes. For example, consideration of equilibrium constraints for coexisting minerals, aqueous fluids, and H_2O-saturated igneous melts permits estimation of the composition of hydrothermal fluids at magmatic temperatures and pressures. Similarly, transition state theory and computer experiments can be used to assess the rates at which silicates react incongruently with aqueous solutions in geochemical processes. Calculations of this kind indicate that these rates are controlled primarily by the chemical affinities of the hydrolysis reactions. As a consequence, the rates of all such irreversible reactions for an assemblage of rock-forming minerals are coupled, and the rate at which each mineral in the reactant assemblage equilibrates is controlled by the last mineral to reach equilibrium. Calculation of interphase mass transfer can be carried out as a function of time by taking account of constraints imposed by conservation of mass and partial and local equilibrium, which permits numerical integration of differential equations representing changes in composition as a function of reaction progress. The results of such calculations can be compared with phase relations observed in rocks to refine the predictions and interpret better the geologic record.

INTRODUCTION

Application of thermodynamics to the study of geochemical processes differs from its application to other kinds of terrestrial processes in several unique ways. For example, many geochemical processes take place over long periods of geologic time in inaccessible regions of the Earth, where temperatures and pressures range from those at the polar ice caps to thousands of degrees and more than a hundred gigapascals in the Earth's interior. Geochemical processes commonly involve many thermodynamic components in a multitude of phases which react with one another in response to changes in the chemical potentials of one or more of the components in response to heat and/or fluid flow, diffusional transfer of material, and/or changes in pressure and temperature. In all cases, the degree to which we achieve insight into these processes depends on the manifestation of chemical and physical events preserved in the geologic record, which may be far from complete and consist of little more than a snapshot of geologic time. It is therefore not surprising that the challenge of understanding geochemical processes far outweighs the rigor available to interpret their consequences. As a result, creative extrapolation has become an integral part of the predictive aspects of theoretical geochemistry.

For the most part, the discipline of theoretical geochemistry consists of borrowed concepts, equations, techniques, and approaches gleaned from chemistry and physics. However, recent efforts to take account of both geologic time and the extreme conditions of temperature and pressure prevailing in the Earth have led to development of theoretical models of geochemical processes which are based in part on explicit recognition of both geologic and thermodynamic constraints on reactions among minerals and aqueous solutions in hydrothermal systems. Among the many thermodynamic aspects of theoretical geochemistry that have been explored in recent years, perhaps the most interesting are those that are at the same time unique and of fundamental importance to our understanding of metasomatic processes. These include high-temperature phase relations in hydrothermal systems and thermodynamic constraints on reaction rates and interphase mass transfer in geochemical processes. The purpose of the present communication is to review recent progress in these areas of research, and to identify fundamental problems that remain to be investigated in our quest for a better understanding of the Earth on which we live.

CONVENTIONS AND NOTATION

The standard state for minerals and H_2O adopted below calls for unit activity of the pure solid or fluid at any temperature or pressure, but that for aqueous species corresponds to unit activity of the species in a hypothetical one molal solution referenced to infinite dilution at any pressure and temperature. All Gibbs free energies and enthalpies generated in the present study for a given pressure (P) and temperature (T) correspond to apparent standard molal Gibbs free energies ($\Delta G^\circ_{P,T}$) and enthalpies ($\Delta H^\circ_{P,T}$) of formation, which are defined by Benson (1) and Helgeson and Kirkham (2) as

$$\Delta G^\circ_{P,T} \equiv \Delta G^\circ_{f,P_r,T_r} + (G^\circ_{P,T} - G^\circ_{P_r,T_r}) \quad (1)$$

and

$$\Delta H^\circ_{P,T} \equiv \Delta H^\circ_{f,P_r,T_r} + (H^\circ_{P,T} - H^\circ_{P_r,T_r}) \quad (2)$$

where $\Delta G^\circ_{f,P_r,T_r}$ and $\Delta H^\circ_{f,P_r,T_r}$ designate the standard molal Gibbs free energy and enthalpy of formation of a given species from its elements in their stable form at a reference pressure (P_r) and temperature (T_r) of 1 bar and 298.15K, and the two parenthetical terms correspond to the differences, respectively, in the values of the standard molal Gibbs free energy and enthalpy of the species at the pressure and temperature of interest and those at P_r,T_r. All thermodynamic properties of aqueous species correspond to conventional properties consistent with regarding the corresponding property of H^+ as zero at all pressures and temperatures. The names and formulas of the minerals considered in the present communication are shown in Table 1.

Table 1. List of minerals and their formulas.

Mineral name	Abbreviation	Formula
albite[a]	AB	$NaAlSi_3O_8$
andalusite	AND	Al_2SiO_5
annite		$KFe_3(AlSi_3O_{10})(OH)_2$
anorthite		$CaAl_2Si_2O_8$
bornite		Cu_5FeS_4
chalcopyrite		$CuFeS_2$
galena		PbS
hematite		Fe_2O_3
K-feldspar[a]	KFL	$KAlSi_3O_8$
magnetite		Fe_3O_4
muscovite	MSC	$KAl_2(AlSi_3O_{10})(OH)_2$
orthoclase	OR	$KAlSi_3O_8$
paragonite	PAR	$NaAl_2(AlSi_3O_{10})(OH)_2$
pyrite		FeS_2
pyrophyllite		$Al_2Si_4O_{10}(OH)_2$
quartz		SiO_2
sillimanite	SIL	Al_2SiO_5
sphalerite		ZnS

[a] The terms albite and K-feldspar refer to $NaAlSi_3O_8$ and $KAlSi_3O_8$ in their equilibrium states of substitutional order/disorder at all temperatures and pressures (Ref. 3).

HIGH-TEMPERATURE PHASE RELATIONS IN HYDROTHERMAL SYSTEMS

The difference in the standard molal Gibbs free energy and enthalpy of a mineral at high pressures and temperatures and those at the reference pressure and temperature can be computed from (Refs. 3—5).

$$G^\circ_{P,T} - G^\circ_{P_r,T_r} = -S^\circ_{P_r,T_r}(T - T_r) + a(T - T_r - T\ln(T/T_r)) + ((c - bT_r^2T)(T - T_r)^2/(2T_r^2T)) + V^\circ_{P_r,T_r}(P - P_r) \quad (3)$$

and

$$H^\circ_{P,T} - H^\circ_{P_r,T_r} = a(T - T_r) + b(T^2 - T_r^2)/2 + c((T_r - T)/(T_rT)) + V^\circ_{P_r,T_r}(P - P_r) \quad , \quad (4)$$

which are consistent with assuming the standard molal volume of the mineral to be independent of pressure and temperature (which is essentially the case in the crust of the Earth) as well as with

$$S^\circ_{P,T} - S^\circ_{P_r,T_r} = a\ln(T/T_r) + b(T - T_r) - c((T^2 - T_r^2)/(2T_r^2T^2)) \quad (5)$$

where $S^\circ_{P,T}$ and $S^\circ_{P_r,T_r}$ stand for the standard molal entropy of the mineral at the subscripted pressures and temperatures, $V^\circ_{P_r,T_r}$ refers to the standard molal volume of the mineral at the reference pressure and temperature, and a, b, and c represent standard molal heat capacity (C°_P) coefficients in the Maier-Kelley power function at 1 bar (Ref. 6), which can be expressed as

$$C^\circ_{P_r} = a + bT - cT^{-2} \quad . \quad (6)$$

Equations representing $G^\circ_{P,T} - G^\circ_{P_r,T_r}$, $H^\circ_{P,T} - H^\circ_{P_r,T_r}$, $S^\circ_{P,T} - S^\circ_{P_r,T_r}$, and C°_P for aqueous species can be written for pressure-temperature regions in which ω is constant (see below) as (Refs. 4, 5, and 7)

$$G^\circ_{P,T} - G^\circ_{P_r,T_r} = -S^\circ_{P_r,T_r}(T - T_r) - c_1(T\ln(T/T_r) - T + T_r) + c_2\left[T - T_r - (T - \theta)\ln\left(\frac{T - \theta}{T_r - \theta}\right)\right] + \frac{2(a_1(T - \theta) + a_3T)(P - P_r) + (a_2(T - \theta) + a_4T)(P^2 - P_r^2)}{2(T - \theta)} - \omega(Z_{P,T} - Z_{P_r,T_r} - Y_{P_r,T_r}(T - T_r)) \quad , \quad (7)$$

$$H^\circ_{P,T} - H^\circ_{P_r,T_r} = (c_1 + c_2)(T - T_r) + c_2\theta \ln\left(\frac{T-\theta}{T_r-\theta}\right) + a_1(P - P_r) + \frac{a_2}{2}(P^2 - P_r^2)$$
$$+ \frac{2a_3T(P-P_r) + a_4T(P^2-P_r^2)}{2(T-\theta)} + \frac{\theta(2a_3T(P-P_r) + a_4T(P^2-P_r^2))}{2(T-\theta)^2}$$
$$+ \omega(TY_{P,T} - T_rY_{P_r,T_r} - Z_{P,T} + Z_{P_r,T_r}) \quad , \tag{8}$$

$$S^\circ_{P,T} - S^\circ_{P_r,T_r} = c_1 \ln(T/T_r) + c_2 \ln\left(\frac{T-\theta}{T_r-\theta}\right) + \frac{\theta(2a_3(P-P_r) + a_4(P^2-P_r^2))}{2(T-\theta)^2}$$
$$+ \omega(Y_{P,T} - Y_{P_r,T_r}) \quad , \tag{9}$$

and

$$C^\circ_P = c_1 + \frac{c_2T}{T-\theta} - \frac{\theta T(2a_3(P-P_r) + a_4(P^2-P_r^2))}{(T-\theta)^3} + \omega T X_{P,T} \quad , \tag{10}$$

which are consistent with

$$V^\circ = a_1 + a_2P + \frac{(a_3 + a_4P)T}{T-\theta} - \omega Q_{P,T} \tag{11}$$

where a_1, a_2, a_3, a_4, c_1, c_2, θ and ω correspond to temperature/pressure-independent coefficients characteristic of a given aqueous species, and the Born functions ($Q_{P,T}$, $X_{P,T}$, $Y_{P,T}$, and $Z_{P,T}$) are defined by

$$Q_{P,T} \equiv \frac{1}{\epsilon_{P,T}}\left(\frac{\partial \ln \epsilon}{\partial P}\right)_T \quad , \tag{12}$$

$$X_{P,T} \equiv \frac{1}{\epsilon_{P,T}}\left(\left(\frac{\partial^2 \ln \epsilon}{\partial T^2}\right)_P - \left(\frac{\partial \ln \epsilon}{\partial T}\right)_P^2\right) \quad , \tag{13}$$

$$Y_{P,T} \equiv \frac{1}{\epsilon_{P,T}}\left(\frac{\partial \ln \epsilon}{\partial T}\right)_P \quad , \tag{14}$$

and

$$Z_{P,T} \equiv -\frac{1}{\epsilon_{P,T}} \quad , \tag{15}$$

where $\epsilon_{P,T}$ represents the dielectric constant of H_2O at the subscripted pressure and temperature.

Except at high pressures and low temperatures, or at pressures and temperatures in the critical region of the system H_2O where the Born coefficient (ω) in Eq. (7) is pressure and temperature dependent (Ref. 8), Eqs. (1) through (14) can be used to describe phase relations among minerals and aqueous species in hydrothermal systems at pressures and temperatures to 5 kb and 1000°C. Refinement of the equation of state for aqueous species (Ref. 8) should soon permit accurate calculation of phase relations throughout this pressure-temperature region. The calculations summarized below were carried out with the aid of computer program SUPCRT (Refs. 3 and 7) using thermodynamic data and parameters taken from Helgeson and Kirkham (2), Helgeson, Delany, Nesbitt, and Bird (3), Helgeson, Kirkham and Flowers (7), and Helgeson (4 and 5). Although uncertainties are difficult to assess in these calculations, comparison of predicted and observed phase relations in both laboratory experiments and geologic systems (e.g., see Refs. 3 and 9—14) indicate that they are small enough to afford close approximation of geologic reality at both high and low temperatures and pressures. The values used in the calculations for the dielectric constant of H_2O and its partial derivatives were generated from equations given by Helgeson and Kirkham (2) for $T < 400$°C and Pitzer's (15) adaptation of the Kirkwood (16) equation for $400° \leqslant T \leqslant 1000$°C (Ref. 8) using thermodynamic properties of the solvent calculated from the Haar, Gallagher, and Kell (17) equation of state for H_2O. These calculations are consistent with the curves shown in Figs. 1 and 2, which represent the dielectric constant of H_2O and the corresponding values of the heat capacity Born function represented by $X_{P,T}$ in Eqs. (10) and (13) as functions of temperatures to 1000°C at pressures $\leqslant 5$ kb. The dashed curves labeled S and L in Fig. 1 represent the solidus for an H_2O-saturated granitic melt (Ref. 18) and the liquidus for an H_2O-saturated granodiorite melt (Ref. 19) respectively. It follows that melts ranging in composition from granites to granodiorites may coexist with silicates and an aqueous phase throughout the pressure-temperature region between the two curves annotated S and L. Note that in this region at pressures $\leqslant 5$ kb the dielectric constant of H_2O is $\lesssim 15$, and it changes only slightly with increasing temperature at constant pressure. In contrast, at lower temperatures ϵ decreases dramatically with increasing temperature at all pressures. In general, ϵ decreases by $\sim$ 10 to 15 units with decreasing pressure from 5 to 0.5 kb over the temperature range $0° < T \leqslant 1000$°C.

It can be deduced from Fig. 2 that the heat capacity Born function (X) decreases dramatically with increasing temperature both above and below the critical point of H_2O. This observation is consistent with the conclusions reached by Helgeson and Kirkham (20) and Gates, Wood, and Quint (21) that values of C°_P for aqueous species in $H_2O_{(liquid)}$ and $H_2O_{(vapor)}$ approach $-\infty$ (Ref. 20) and ∞ (Ref. 21), respectively, at the critical point of H_2O. Note in Fig. 2 that the

influence of the critical phenomenon on the variation of X with temperature decreases with increasing pressure and essentially dampens out above 2 kb. These observations are consistent with the configurations of the curves shown in Fig. 3 for C°_{P,Na^+} as a function of temperature to 1000°C at pressures $\leqslant$ 5 kb, where it can be seen that the calculated values of C°_{P,Na^+} range from ~ -150 to $\sim$ 50 cal mole^{-1} K^{-1} at 1 kb. In contrast, at lower pressures above the critical pressure of H_2O, the calculated range exceeds many thousands of cal mole^{-1} K^{-1}, and from 2 – 5 kb it diminishes to $\lesssim$ 30 cal mole^{-1} K^{-1}. Because the standard molal heat capacities of Na^+ shown in Fig. 3 were generated assuming ω in Eq. (7) to be constant, they are subject to considerable uncertainty at pressures $\lesssim$ 1 kb and temperatures $\gtrsim$ 300°C. Consideration of recent experimental data indicates that Eq. (10) results in values of C°_P in this pressure-temperature region that are too negative, which has prompted revision (Ref. 8) of the equations of state represented by Eqs. (10) and (11). Nevertheless, the curves shown in Fig. 3 are qualitatively correct and serve to illustrate the general configuration of C°_P for aqueous species at high temperatures and pressures.

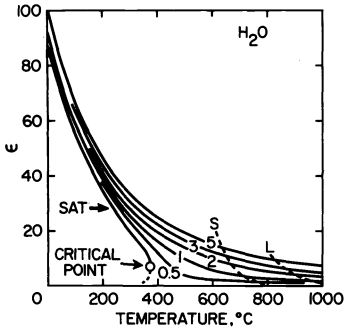

Fig. 1. Dielectric constant of $H_2O(\epsilon)$ as a function of temperature at constant pressure (labeled in kb) calculated from equations and parameters given by Helgeson and Kirkham (2) and Pitzer's (15) adaptation of the Kirkwood (16) equation (see text). SAT refers to the vapor-liquid equilibrium curve for H_2O. the dashed curves labeled S and L designate the solidus and liquidus for H_2O-saturated granitic and granodioritic melts, respectively (Refs. 18, 19).

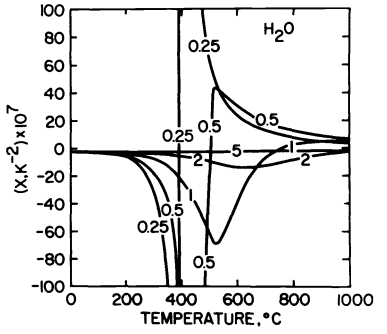

Fig. 2. Heat capacity Born function (X) defined by Eq. (13) as a function of temperature at constant pressure (labeled in kb) calculated from equations and parameters given by Helgeson and Kirkham (2) and Pitzer's (15) adaptation of the Kirkwood (16) equation (see text).

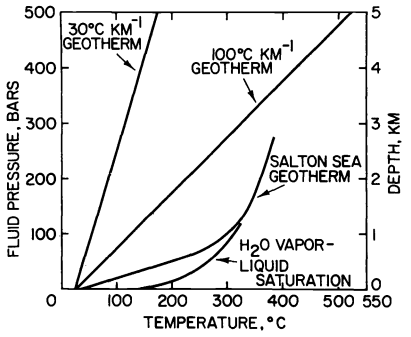

Fig. 4. Geothermal profiles used to generate the curves shown in Figs. 5 through 8. The profile labeled Salton Sea Geotherm corresponds to that in the No. 1 IID Well (Ref. 43).

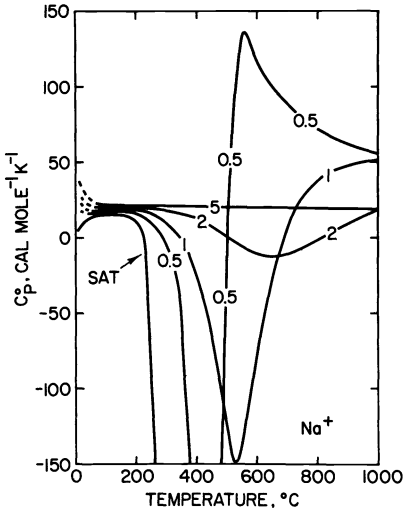

Fig. 3. Standard molal heat capacity of Na^+ as a function of temperature to 1000°C at constant pressure (labeled in kb) calculated from Eq. (10) using values of X shown in Fig. 2 and parameters taken from Ref. 7 (see text). SAT refers to the vapor-liquid equilibrium curve for H_2O.

Although the fluid pressure (P_f) in a hydrothermal fissure commonly differs from the geostatic pressure (P_g), it follows from Gibbs' (22) Eq. (385) that equilibrium between a mineral in a state of elastic deformation and homogeneous strain subjected to P_g at the fluid/rock interface and the aqueous species in the fluid can be described accurately by

$$K = \exp(-\Delta G_r^\circ/RT) \tag{16}$$

only if the thermodynamic consequences of elastic deformation of the solid are negligible (which is true in the crust of the Earth) and the standard molal Gibbs free energy of the reaction (ΔG_r°) is calculated for P_f and T (Ref. 23). Under these circumstances, Eq. (16) applies to both hydrostatic and nonhydrostatic states of stress in hydrothermal systems. Eq. (16) with ΔG_r° computed at P_f and T is consistent with Gibbs' observations that no unique Gibbs free energy can be assigned to a mineral in a state of nonhydrostatic stress, and that the chemical potentials of a given component in the mineral and adjacent fluid are equal at equilibrium only if the system is in a state of hydrostatic stress (Ref. 23).

A number of examples of equilibrium constants calculated from Eqs. (1), (3), (7), (14), (15), and (16) for reversible reactions between a flowing hydrothermal solution and its mineralogic environment along the various temperature-fluid pressure profiles shown in Fig. 4 are depicted in Figs. 5 through 8. The electrostatic and thermodynamic properties of H_2O employed in the calculations were generated from equations and parameters taken from Refs. 2 and 17, respectively. The designations of the curves in Figs. 5 through 8 as galena, sphalerite, pyrite, and chalcopyrite represent the following reactions:

$$\underset{(galena)}{PbS} + H^+ \rightleftarrows Pb^{++} + HS^- \ , \tag{17}$$

$$\underset{(sphalerite)}{ZnS} + H^+ \rightleftarrows Zn^{++} + HS^- \ , \tag{18}$$

$$\underset{(pyrite)}{FeS_2} + H_2O \rightleftarrows Fe^{++} + 7/4\,HS^- + 1/4\,SO_4^{--} + 1/4\,H^+ \ , \tag{19}$$

and

$$\underset{(chalcopyrite)}{CuFeS_2} + 7/8\,H^+ + 1/2\,H_2O \rightleftarrows Cu^+ + Fe^{++} + 15/8\,HS^- + 1/8\,SO_4^{--} \ , \tag{20}$$

Owing to the relatively low geothermal gradient shown in Fig. 5, all of the curves in the figure are monotonic to a depth of 5 kb and the activity product of galena is smaller than that of sphalerite over the entire depth interval. In contrast, it can be seen in Figs. 6 through 8 that all of the curves for the other geothermal gradients in Fig. 4 exhibit extrema at depths ranging from 0.1 to 3.0 km, depending on the reaction and the geotherm. In the case of sphalerite and pyrite along the 100°C km^{-1} geotherm in Fig. 6, the extrema are broad and gentle in configuration. As a result, little change occurs in the relative stabilities of these minerals between $\sim$ 1.5 and 3.0 km, which is not true of galena and chalcopyrite. Note in Figs. 6 through 8 that the curves for galena and sphalerite cross each other with increasing depth and temperature. As a consequence, galena would be expected to replace sphalerite at shallow depths, but the opposite should occur at deeper depths.

The curves shown in Figs. 5 through 8 are typical of mineral hydrolysis reactions in general. The extrema in the curves are an inevitable consequence of the critical phenomenon exhibited by the solvent. In all cases the minerals become more stable at high temperatures relative to their dissolved counterparts. However, because aqueous complexes also become more stable relative to dissociated species at high temperatures (Refs. 24—28), the solubilities of most minerals increase rather than decrease with increasing temperature.

Curves representing the relative stabilities of pyrite and chalcopyrite in a hydrothermal system are shown in Fig. 9 as a function of temperature to 1000°C for pressures ranging from those corresponding to vapor-liquid equilibrium for H_2O (SAT) to 5 kb. It can be seen in Fig. 9 that all of the curves representing log K for the reaction shown in the figure exhibit a maximum, except that for 5 kb. At SAT $< P \leq$ 3 kb, chalcopyrite becomes more stable relative to pyrite with increasing temperature at high temperatures. However, it is apparent in Fig. 9 that the curve for 0.5 kb exhibits a minimum between 750° and 800°C. The minimum occurs in response to the change in $\Delta G^\circ_{Fe^{++}}$ with increasing temperature. It can be seen in Fig. 10 that $\Delta G^\circ_{Fe^{++}}$ becomes positive above $\sim$ 460°C at 0.5 kb. As it becomes increasingly positive at higher temperatures, it causes the log K curve for 0.5 kb in Fig. 9 to minimize. The behavior exhibited by $\Delta G^\circ_{Fe^{++}}$ in Fig. 10 is also exhibited by ΔG° for Mn^{++}, Zn^{++}, and Cu^{++}. In contrast, note in Fig. 10 that $\Delta G^\circ_{Mg^{++}}$ remains negative at pressures $\geqslant$0.5 kb to 1000°C.

As indicated above, the region between the dashed curves annotated S and L in Figs. 9 and 10 represents the pressure-temperature region in which H_2O-saturated melts of granite to granodiorite composition may coexist with silicates and an aqueous phase in magma-hydrothermal systems. It follows from the configuration of the curves in Fig. 9 that the higher a granitic melt intrudes in the Earth's crust the more stable is chalcopyrite relative to pyrite at the solidus temperatures. Complexing of Cu^+ and Fe^{++} (which are the dominant valence states of copper and iron in hydrothermal solutions—Ref. 10) notwithstanding, it thus appears that shallow emplacement of porphyry copper intrusives is a requisite for formation of copper-rich protore, which would otherwise be copper-poor and iron-rich at greater depths where the copper remains in solution. Fluid inclusion studies indicate that these solutions almost invariably consist of relatively concentrated electrolyte solutions in which NaCl and to a lesser extent KCl, $MgCl_2$ and $CaCl_2$ are the dominant solute components. Nevertheless, the activity of H_2O in these solutions departs only slightly from unity ($\sim$ 0.9 < a_{H_2O} < 1.0) at high temperatures and pressures for concentrations of NaCl $\leqslant$ 3 m (Refs. 28 and 29).

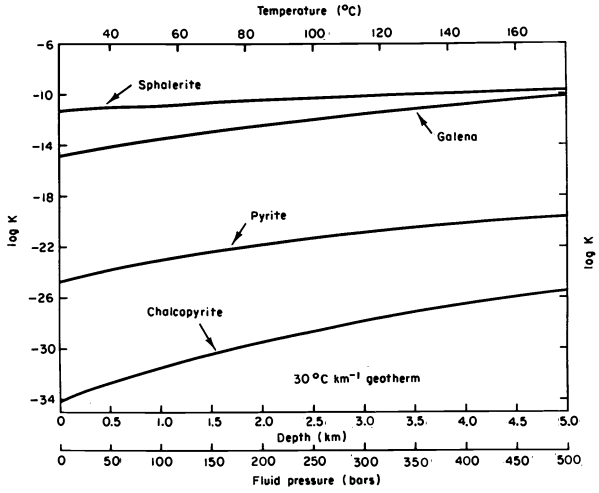

Fig. 5. Logarithm of the equilibrium constant for reactions (17) through (20) at temperatures and pressures corresponding to those along the 30°C km^{-1} geotherm in Fig. 4 calculated from Eqs. (1), (3), (7), (15), and (16) using values of ϵ shown in Fig. 1 and thermodynamic data and parameters taken from Refs. 2, 3, 4, 5, 7, and 17.

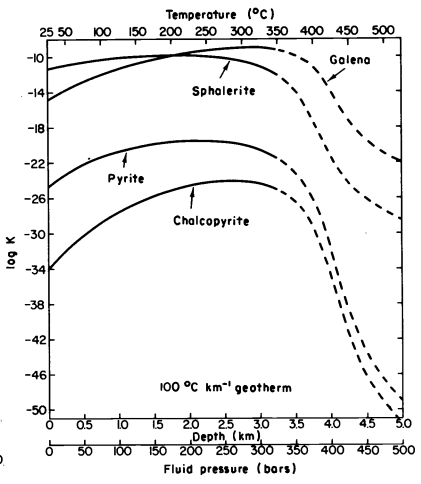

Fig. 6. Logarithm of the equilibrium constant for reactions (17) through (20) at temperatures and pressures corresponding to those along the 100°C km^{-1} geotherm in Fig. 4 calculated in the manner described in the caption of Fig. 5. The dashed curves indicate higher uncertainty than their solid counterparts.

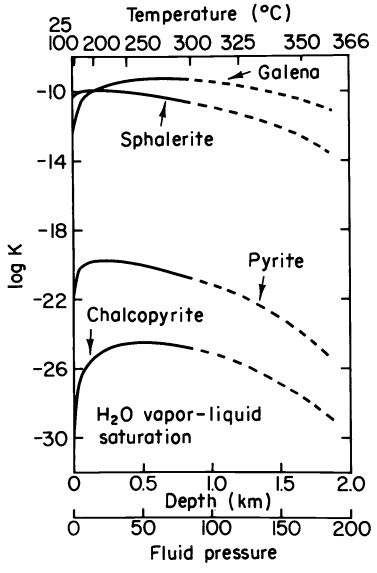

Fig. 7. Logarithm of the equilibrium constant for reactions (17) through (20) at temperatures and pressures corresponding to those along the vapor-liquid equilibrium curve for H_2O in Fig. 4 calculated in the manner described in the caption of Fig. 5. The dashed curves indicate higher uncertainty than their solid counterparts.

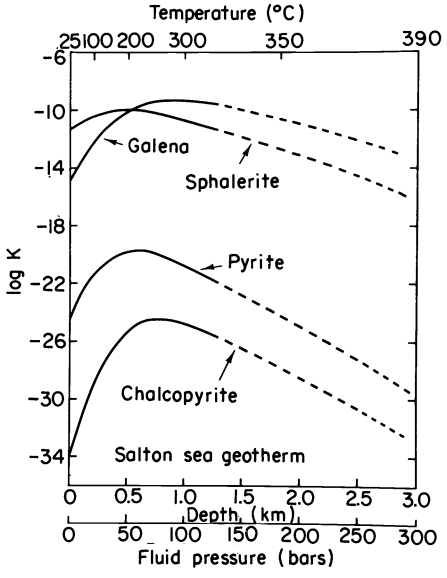

Fig. 8. Logarithm of the equilibrium constant for reactions (17) through (20) at temperatures and pressures corresponding to those along the Salton Sea geotherm in Fig. 4 calculated in the manner described in the caption of Fig. 5. The dashed curves indicate higher uncertainty than their solid counterparts.

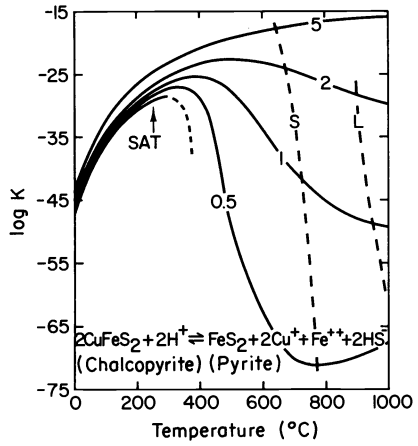

Fig. 9. Logarithm of the equilibrium constant for the reaction shown above as a function of temperature at constant pressure (labeled in kb) calculated in the manner described in the caption of Fig. 5. SAT refers to the vapor-liquid equilibrium curve for H_2O, which is dashed where the position of the curve is extrapolated. The dashed curves labeled S and L designate the solidus and liquidus for H_2O-saturated granitic and granodioritic melts, respectively (Refs. 18, 19).

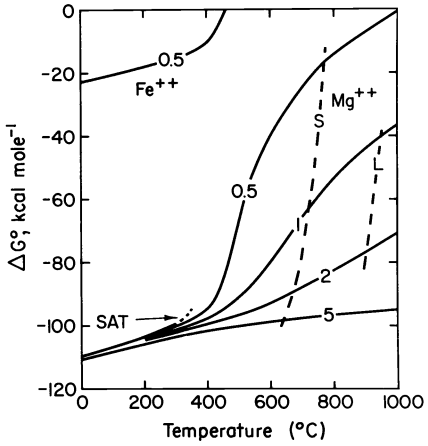

Fig. 10. Apparent standard molal Gibbs free energy of formation of Fe^{++} and Mg^{++} as a function of temperature at constant pressure (labeled in kb) calculated from Eqns. (1), (7), and (15), using values of ϵ shown in Fig. 1 and thermodynamic data and parameters taken from Ref. 7 (see caption of Fig. 9).

Hydrothermal phase relations among minerals coexisting with an aqueous electrolyte solution and quartz in rocks of granitic composition can be depicted in logarithmic activity diagrams for the system Na_2O–K_2O–Al_2O_3–SiO_2–H_2O–HCl in terms of log (a_{Na^+}/a_{H^+}) and log (a_{K^+}/a_{H^+}) at constant temperature, pressure, and $a_{H_2O} \approx 1$. A series of such diagrams generated in the manner described in Ref. 30 is shown in Fig. 11 for temperatures from 400° to 900°C at 2 kb.

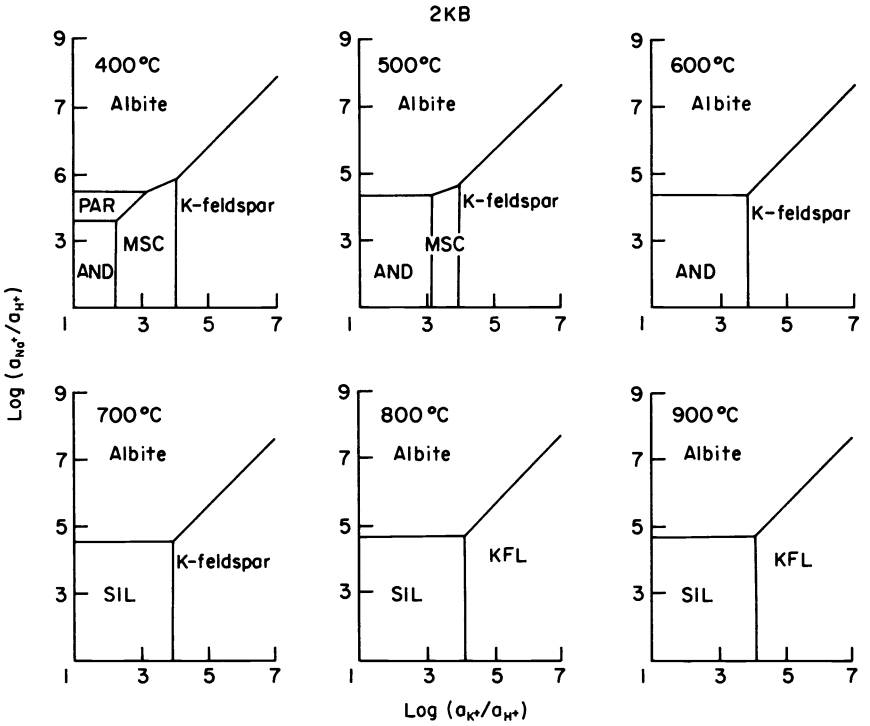

Fig. 11. Logarithmic activity diagrams for the system Na_2O–K_2O–Al_2O_3–SiO_2–H_2O–HCl in the presence of quartz at 2 kb and temperatures from 400° to 900°C. The diagrams were generated for unit activity of H_2O from equilibrium constants calculated in the manner described in the caption of Fig. 5 (see text).

Diagrams of this kind can be used together with dissociation constants and activity coefficients (e.g., Refs. 7 and 24 through 29—see also Figs. 12 and 13) to assess the compositions of hydrothermal solutions coexisting with granitic mineral assemblages at high pressures and temperatures. For example, taking account of the curves for 2 kb in Figs. 12 and 13, together with conservation of mass constraints, activity coefficients, and calculated phase relations like those shown in Fig. 11 (Refs. 2, 3, 30, 48) indicates that a sanidine solid solution with a composition corresponding to $Or_{50}Ab_{50}$ in equilibrium with quartz, andalusite, and an H_2O-saturated granitic melt may coexist with a 2 molal NaCl/KCl solution with a pH of ~ 6.5 at 675°C and 2 kb. If it were not for the high degree of formation of NaCl° and KCl° in solution under these conditions, the pH of the aqueous phase would be much lower.

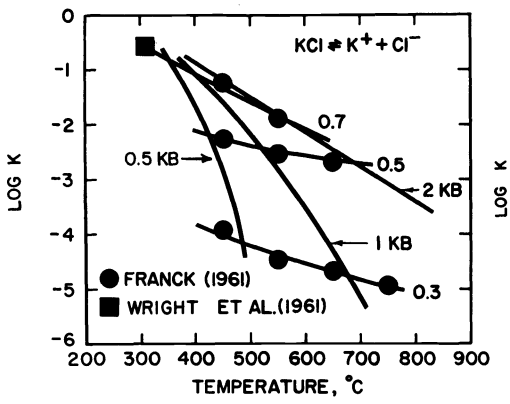

Fig. 12. Logarithm of the dissociation constant for KCl as a function of temperature at constant density (labeled in g cm^{-3}) or pressure (labeled in kb). Franck (1961) and Wright et al. (1961) correspond to Refs. 44 and 45.

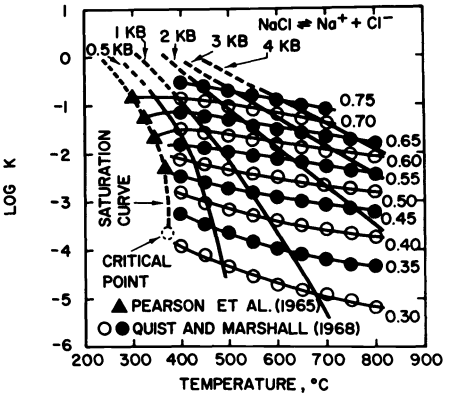

Fig. 13. Logarithm of the dissociation constant for NaCl as a function of temperature at constant density (labeled in g cm^{-3}) or pressure (labeled in kb). Pearson et al. (1965) and Quist and Marshall (1968) correspond to Refs. 46 and 47. The dashed saturation curve and critical point refer to the vapor-liquid equilibrium curve and critical point for H_2O, respectively.

It can be seen in Figs. 12 and 13 that the logarithms of the dissociation constants of KCl and NaCl decrease dramatically with increasing temperature at pressures $\lesssim$ 2 kb, but they are nevertheless roughly equivalent at high temperatures. It follows from this observation together with the Margules expansion for alkali feldspar solid solutions (Ref. 48) and the curves shown in Fig. 14 that equilibrium among a sanidine solid solution with a composition corresponding to $Or_{50}Ab_{50}$, an H_2O-saturated granitic melt, and an aqueous NaCl/KCl solution at 0.5 kb and ~ 770°C requires the total concentration of KCl to be ~ 5 times the total concentration of NaCl in the aqueous phase. In contrast, the total concentration of NaCl exceeds that of KCl for equilibrium among K-feldspar, albite, and an aqueous phase by more than an order of magnitude at all pressures and temperatures below ~ 400°C. It follows that cooling of a granitic pluton in the presence

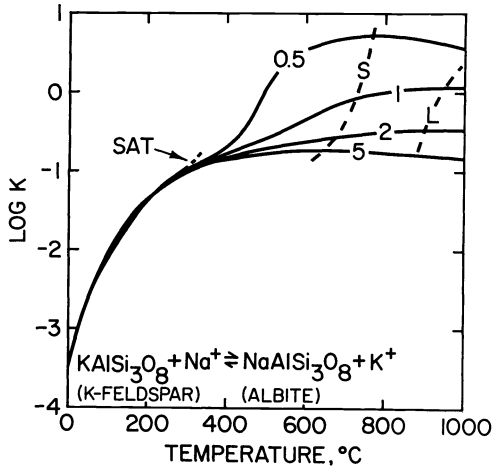

Fig. 14. Logarithm of the equilibrium constant for the reaction shown in the figure as a function of temperature at constant pressure (labeled in kb) calculated in the manner described in the caption of Fig. 5 (see caption of Fig. 9).

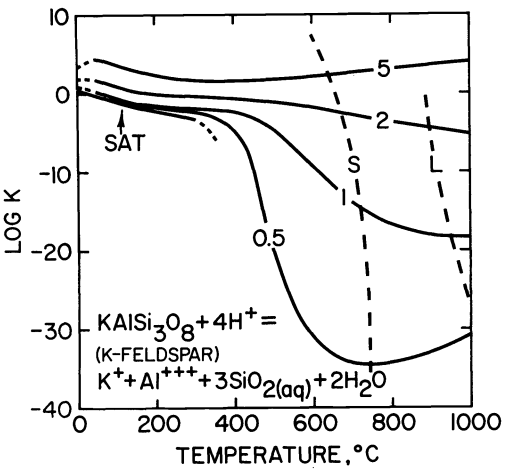

Fig. 15. Logarithm of the equilibrium constant for the reaction shown above as a function of temperature at constant pressure (labeled in kb) calculated in the manner described in the caption of Fig. 5 (see caption of Fig. 9).

of an aqueous chloride solution from the solidus to a lower temperature should result in precipitation of hydrothermal K-feldspar at the expense of albite over the entire cooling path. However, if the pluton intrudes into the upper crust so that $P_f \leq 0.5$ kb, the bulk of this precipitation should occur as the pluton cools from 600° to 400°C.

The curves depicted in Fig. 14 are consistent with those for the hydrolysis reaction shown in Fig. 15. It follows from the configuration of the curves in the latter figure that (with the exception of low pressures and high temperatures), increasing temperature at pressures $\leq$ 2 kb leads to decreasing pH for solutions in equilibrium with K-feldspar. The same observation holds if quartz is also present in the system. The configurations of the curves for K-feldspar hydrolysis in Fig. 15 are similar to those representing chalcopyrite-pyrite equilibrium in Fig. 9. As in the case of the influence of the change in $\Delta G^\circ_{Fe^{++}}$ with increasing temperature on the configuration of the curve for 0.5 kb in Fig. 9, the high-temperature minimum in the curve for 0.5 kb in Fig. 15 arises from the fact that $\Delta G^\circ_{Al^{+++}}$ increases and becomes positive with increasing temperature in the upper crust of the Earth.

Apparent standard molal Gibbs free energies of formation of Na^+ and Cl^- are plotted as functions of temperature to 1000°C at pressures $\leqslant$ 5 kb in Figs. 16 and 17, respectively, where it can be seen that the two ions exhibit dramatically different behavior with increasing temperature. Taking account of the curves shown in these figures and those for the dissociation constant of $NaCl^\circ$ in Fig. 12 permits calculation of $\Delta G^\circ_{NaCl^\circ}$, which is depicted in Fig. 18. It can be seen in Fig. 18 that the curve for 1 kb exhibits a maximum at the intersection of the curve with that for the solidus of an H_2O-saturated granitic melt. Similar extrema occur at lower pressures and higher values of $\Delta G^\circ_{NaCl^\circ}$ than those shown in the figure.

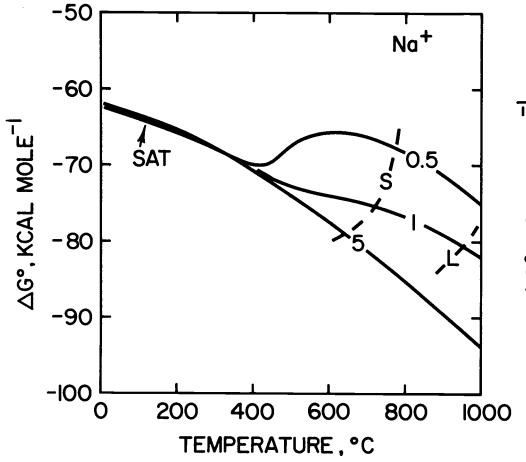

Fig. 16. Apparent standard molal Gibbs free energy of formation of Na^{++} as a function of temperature at constant pressure (labeled in kb) calculated in the manner described in the caption of Fig. 10 (see caption of Fig. 9).

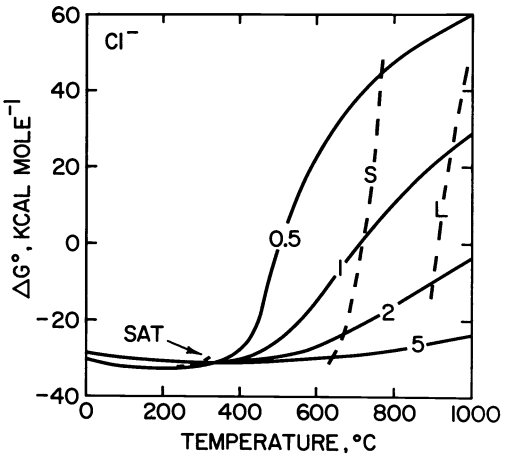

Fig. 17. Apparent standard molal Gibbs free energy of formation of Cl^- as a function of temperature at constant pressure (labeled in kb) calculated in the manner described in the caption of Fig. 10 (see caption of Fig. 9).

Apparent standard molal Gibbs free energies of formation of Na^+ and Cl^- are plotted as functions of temperature to 1000°C at pressures $\leqslant$ 5 kb in Figs. 16 and 17, respectively, where it can be seen that the two ions exhibit dramatically different behavior with increasing temperature. Taking account of the curves shown in these figures and those for the dissociation constant of $NaCl^\circ$ in Fig. 12 permits calculation of $\Delta G^\circ_{NaCl^\circ}$, which is depicted in Fig. 18. It can be seen in Fig. 18 that the curve for 1 kb exhibits a maximum at the intersection of the curve with that for the solidus of an H_2O-saturated granitic melt. Similar extrema occur at lower pressures and higher values of $\Delta G^\circ_{NaCl^\circ}$ than those shown in the figure.

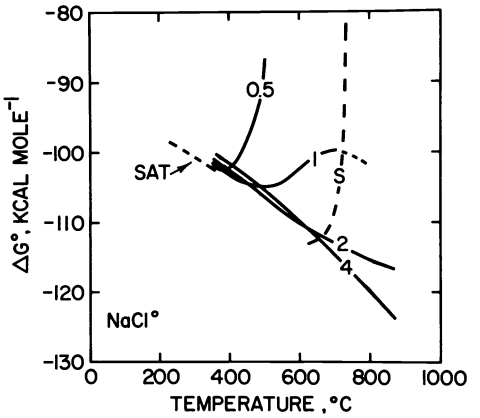

Fig. 18. Apparent standard molal Gibbs free energy of the aqueous NaCl molecule ($NaCl^\circ$) as a function of temperature at constant pressure (labeled in kb) calculated from Eq. (16) using values of log K_{NaCl°, $\Delta G^\circ_{Na^+}$, and $\Delta G^\circ_{Cl^-}$ taken from Figs. 13, 16, and 17 (see caption of Fig. 9).

THERMODYNAMIC CONSTRAINTS ON REACTION RATES IN GEOCHEMICAL PROCESSES

Consideration of kinetic data for the hydrolysis of feldspar, quartz, enstatite, and other silicates at both high and low temperatures using van't Hoff's rule and transition state theory indicates that the steady-state rates of both congruent and incongruent dissolution reactions for silicates can be represented by (Refs. 31—34)

$$\frac{d\xi}{dt} = k'\bar{s}\left(\prod_i a_{H^+}^{-\hat{n}_{H^+}}\right)(1 - \exp(-A/\sigma RT)) \tag{21}$$

which can be rearranged and integrated for constant $s/\bar{s}$ (see below) to give

$$t = t^\circ + k'^{-1}\int_0^\xi \left(\bar{s}^{-1}\prod_i a_{H^+}^{\hat{n}_{H^+}}/(1-\exp(-A/\sigma RT))\right)d\xi \tag{22}$$

where t denotes time in seconds, ξ designates the overall progress variable for the process (Refs. 35 and 37) in moles, t° designates the time at which $\xi = 0$, a_{H^+} represents the activity of the hydrogen ion in the aqueous phase (which is dimensionless), $\bar{s}$ refers to the total surface area of the reactant mineral in cm^2, $\hat{n}_{H^+}$ denotes the reaction coefficient of the hydrogen ion (which is dimensionless, temperature independent, and positive if H^+ is a product, but negative if it is a reactant) in the reversible reaction corresponding to formation of one mole of the activated complex on the surface of the reactant mineral, R designates the gas constant in cal $mole^{-1}$ K^{-1}, T represents temperature in K, A stands for the chemical affinity of the overall reaction in cal $mole^{-1}$, σ refers to the average stoichiometric number, which in this case is equal to the ratio of the rate of decomposition of the activated complex to that of the overall reaction, and k' denotes the apparent rate constant for the reaction in moles cm^{-2} sec^{-1}, which can be expressed as

$$k' = ks/\bar{s} \tag{23}$$

where s refers to the effective surface area of the reactant mineral (which corresponds to the total area of active (reactant) sites exposed to the aqueous phase) in cm^2, and k stands for the transition state rate constant, which is given by

$$k \equiv \frac{\alpha K^\ddagger kT}{\sigma\bar{\gamma}^\ddagger h} \tag{24}$$

where α refers to the transmission coefficient for the activated complex (which corresponds to the probability that the complex will decompose into products, rather than reactants), $K^\ddagger$ stands for the equilibrium constant for the reaction representing reversible formation from the reactants of one mole of the activated complex, k corresponds to Boltzmann's constant, h designates Planck's constant, and $\bar{\gamma}^\ddagger$ denotes the activity coefficient of the activated complex.

Values of $\hat{n}_{H^+}$ for K-feldspar and albite in Eqs. (21) and (22) range from $\sim$ 0.4 and 0 for highly alkaline and intermediate pH solutions to -1 for acid solutions (Ref. 33). Corresponding values for enstatite, diopside, and forsterite in acid solutions are -0.6, -0.75, and -1.1, respectively (Ref. 34). Equations (21) and (22) for K-feldspar and albite are consistent with rate-limiting decomposition of a single activated complex on the reactant surface with stoichiometries corresponding to a protonated, hydrated, or hydroxylated feldspar, depending on the solution pH. The active sites most likely correspond to dislocation outcrops and/or risers between cleavage surfaces. Even at high temperatures, the rate of hydrolysis of K-feldspar is apparently controlled by surface reactions at active sites, rather than by diffusional transfer of material in the aqueous phase (Ref. 33).

Thermodynamics contributes to Eqs. (21) and (22) in three important ways: 1) through the dependence of the apparent rate constant on the equilibrium constant for reversible formation of the activated complex on the surface of the reactant mineral, 2) through the partial dependence in the reaction process of changes in solution pH on local and/or partial equilibrium states, all of which are coupled, and 3) through the dependence of chemical affinity on solution composition and the equilibrium constant of the overall reaction (K), which is given by

$$A = RT\ln(K/Q) \quad , \tag{25}$$

where Q is defined by

$$Q \equiv a_i^{-1}\prod_l a_l^{\hat{n}_l} \tag{26}$$

where a_l and a_i denote the activities of the lth aqueous species and the ith thermodynamic component of the reactant mineral (which is unity if the mineral is stoichiometric) and $\hat{n}_l$ represents the reaction coefficient of the lth aqueous species in the overall hydrolysis reaction, which is negative for reactants and positive for products. For these reasons (as well as others), Eq. (21) can be regarded as a thermodynamic rate law for mineral hydrolysis in geochemical processes.

Calculated rates of K-feldspar hydrolysis for the intermediate and acid pH region are shown in Fig. 19 for temperatures from 25° to 500°C. The rates shown in the figure correspond to apparent rates far from equilibrium where the chemical affinity term in Eq. (21) is negligible. The apparent rates were calculated from Eq. (21) and

$$r' = \frac{1}{\bar{s}}\frac{d\xi}{dt} \tag{27}$$

using apparent rate constants taken from Helgeson Murphy, and Aagaard (33). These rate constants are consistent with the linear curves shown in Fig. 20, which were generated by taking account of transition state theory assuming the heat capacity of activation to be zero (Ref. 33).

It can be seen in Fig. 19 that rates of feldspar hydrolysis far from equilibrium at 25°C depend on solution pH only at pH $\leq$ 2.9. However, with increasing temperature, the transition pH separating the pH-dependent from the pH-independent rate regimes increases according to 10.6 − (2300/T). Taking account of the fact that phase relations and fluid inclusions in hydrothermal systems are consistent with pH values of ~ 3 — 5 at temperatures below ~ 300°C (Refs. 9 and 10), it follows that the rates of feldspar hydrolysis in such systems are pH-dependent.

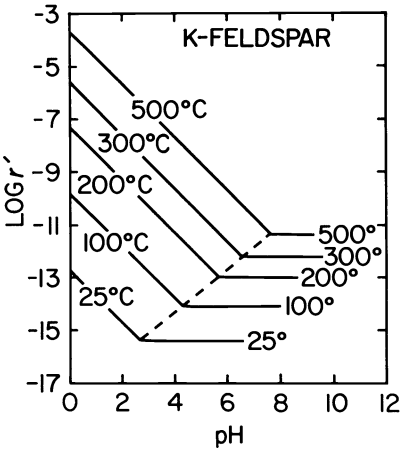

Fig. 19. Apparent rate of K-feldspar hydrolysis far from equilibrium as a function of pH at constant temperature computed from Eqns. (21) and (27) using rate constants generated from the curves shown in Fig. 20 (Ref. 33).

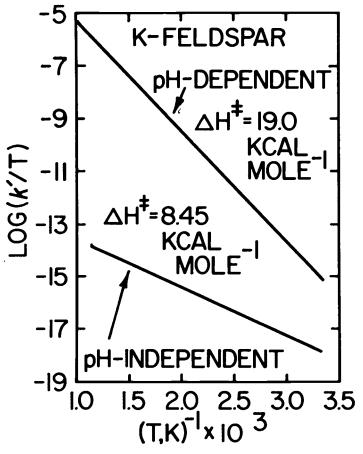

Fig. 20. Logarithm of the quotient of the apparent rate constant for the hydrolysis of K-feldspar and temperature in K as a function of reciprocal temperature (Ref. 33).

Changes in mineral and solution composition accompanying reactions in geochemical processes can be computed as functions of time and surface area by first specifying the initial composition of the aqueous phase and calculating the activities and molalities of all aqueous species in the solution at the outset of the reaction process. The calculations are carried out by taking account of constraints imposed by conservation of mass and homogeneous equilibrium in the aqueous solution, which may or may not coexist with an equilibrium mineral assemblage. The activities and molalities of the aqueous species are computed with the aid of dissociation constants and an extended Debye-Hückel equation. A given set of reactant minerals is then specified, each of which is initially out of equilibrium with the aqueous phase. As these minerals react with the solution, relative reaction rates are computed at each stage of reaction progress. If the solution becomes saturated with one or another mineral, which may or may not be destroyed at a later stage of reaction progress, the incongruent reaction product is assumed to precipitate or dissolve reversibly, which is consistent with both field and laboratory observations that dissolution of the original reactant minerals is rate limiting in geochemical processes (Refs. 31, 32, and 34). Although precipitation of a reaction product requires the solution to be supersaturated with respect to the mineral, the degree of supersaturation is negligible compared to the extent of interphase mass transfer during the precipitation process.

The calculations described above, together with a numerical integration computer routine permit evaluation of a statement of Eq. (22) for each reactant mineral at incremented stages of reaction progress (Ref. 32). As a result, all changes in solution composition and the mass of each mineral produced and destroyed in a geochemical process can be expressed as explicit functions of time and surface area. Calculations of this kind were carried out for reaction of a "typical" hydrothermal solution (Ref. 10) with a granitic mineral assemblage at 300°C and 100 bars. Some of the results are shown in Fig. 21, where the mass of minerals produced and destroyed during reaction of K-feldspar, plagioclase (represented by the relative abundances of albite and anorthite), quartz, and biotite (represented by annite) with an aqueous electrolyte solution containing small concentrations of copper, iron, and zinc species (as well as other species present in minor concentrations) are depicted as a function of time. The calculations were carried out with the aid of a modified version of Wolery's EQ 3/6 computer code (Ref. 36), using rate constants taken from Helgeson Murphy, and Aagaard (33) and Rimstidt and Barnes (38). The rate constant of annite was taken to be equal to that of K-feldspar and the total surface area of the reactants was set to a constant and conservative value of 100 cm^2 (kg $H_2O)^{-1}$. For the sake of clarity in presentation, no provision for solid solutions was incorporated in the calculations. However, comparable calculations can be carried out for minerals of variable composition by taking account of equations representing intracrystalline mixing and exchange of atoms on crystallographic sites like those summarized by Helgeson and Aagaard (39).

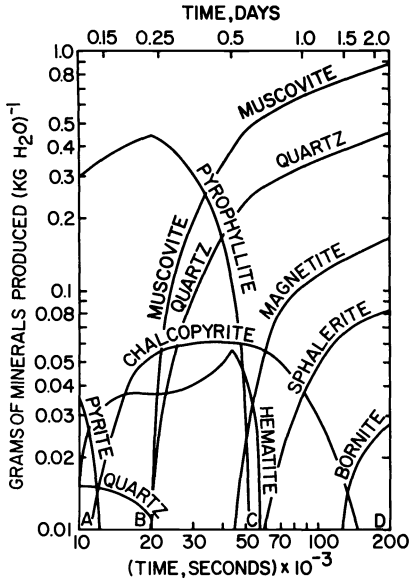

Fig. 21. Grams of minerals produced and destroyed as a function of time during reaction of a granitic mineral assemblage with a hydrothermal ore-forming solution at 300°C and 100 bars (see text).

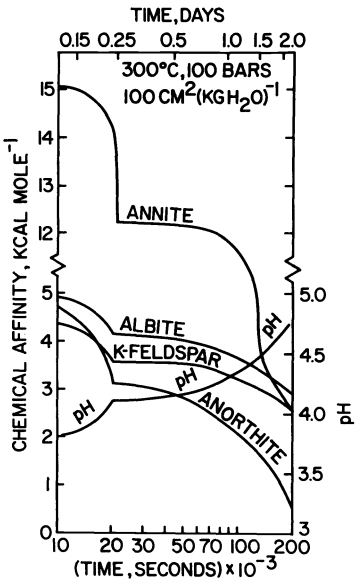

Fig. 22. Chemical affinity (Eq. 25) as a function of time for the reaction described in the caption of Fig. 21 (see text). Albite and anorthite refer to the components of plagioclase and annite represents biotite.

It can be seen in Fig. 21 that the reaction process represented by the computer experiment is exceedingly rapid at 300°C and 100 bars, which is a consequence in part of the low pH (3) of the initial reactant solution. Within an hour pyrite precipitates, but it is almost immediately replaced by chalcopyrite, which then forms along with pyrophyllite and hematite at the expense of K-feldspar, plagioclase, biotite, and quartz in the early stages of reaction progress along reaction segment AB in Fig. 21. The appearance of muscovite at B causes subsequent destruction of pyrophyllite and precipitation of quartz. In the vicinity of C in Fig. 21, magnetite begins to replace hematite and then sphalerite begins to replace chalcopyrite, reactant solution. Muscovite, quartz, magnetite, sphalerite, and bornite then continue to form at the expense of K-feldspar, plagioclase, and biotite as they continue to react irreversibly and incongruently with the aqueous phase. Although not shown in Fig. 21, in a matter of months or less K-feldspar and annite equilibrate, and the plagioclase reaction reaches a quasistatic state in which the reaction rate becomes proportional to the chemical affinity of the overall reaction (Refs. 31 and 32). Because the chemical affinity of the plagioclase reaction is $\lesssim$ 500 cal mole^{-1} in the quasistatic state, the reaction proceeds slowly toward equilibrium with continued reaction progress.

The changes in solution pH and the chemical affinities of the irreversible reactions accompanying the incongruent reaction process described above are highly sensitive to the appearance or disappearance of reaction products. For example, note in Fig. 22 the time derivative of the chemical affinity for the hydrolysis of annite abruptly changes to zero as soon as muscovite starts to precipitate at the expense of pyrophyllite. It follows that rates of hydrolysis in the vicinity of equilibrium where the rates of reaction become proportional to the chemical affinities of the irreversible reactions (Ref. 31) may be affected substantially by formation or destruction of reaction products, as well as by the sequential equilibration of the reactant minerals. Because all of the reactions are coupled by common species, their rates are not independent of one another. As a consequence, the rate at which a given reactant mineral equilibrates is determined by the rate at which the last mineral to equilibrate reaches equilibrium and the intermediate reaction products act as regulators on the rate at which this is achieved (Ref. 32).

The sequence of events corresponding to ABCD in Fig. 21 is depicted as reaction path ABCD in the logarithmic activity diagrams shown in Figs. 23 and 24. With continued reaction along reaction path segment CD, the solution first equilibrates with K-feldspar, and then with annite. In the process, a_{Na^+}/a_{K^+} changes only slightly, but $a_{Fe^{++}}/a^2_{K^+}$ increases substantially.

The time interval represented by ABDC in Figs. 21, 23, and 24 spans $\sim$ 2 x 10^5 seconds. The specific surface area stipulated in the computer experiment (100 cm^2 (kg H_2O)$^{-1}$) corresponds for a roughness factor of one to the surface area of the walls of a segment of a fissure 10 cm long, 5 cm deep, and 20 cm wide. Assuming diffusional transfer in the aqueous phase to be rapid relative to the flow rate, the limiting flow rate required for the events portrayed in Fig. 22 to occur within this 1 liter volume of the fissure is $\lesssim$ 1.6 liters, year^{-1}, which is consistent with a horizontal flow velocity of $\lesssim$ 16 cm year^{-1}. Under these circumstances, 990 cm^3 or more of the hydrothermal fluid in the original liter volume

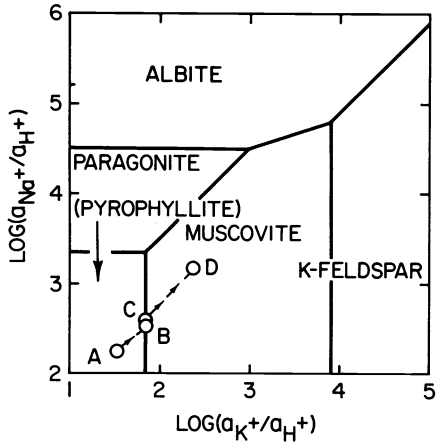

Fig. 23. Logarithmic activity diagram for the system Na_2O–K_2O–Al_2O_3–SiO_2–H_2O–HCl in the presence of quartz for unit activity of H_2O at 300°C and 100 bars. The diagram was generated from equilibrium constants calculated in the manner described in the caption of Fig. 5 (see text). Reaction path ABCD corresponds to the sequence of events depicted in Fig. 21.

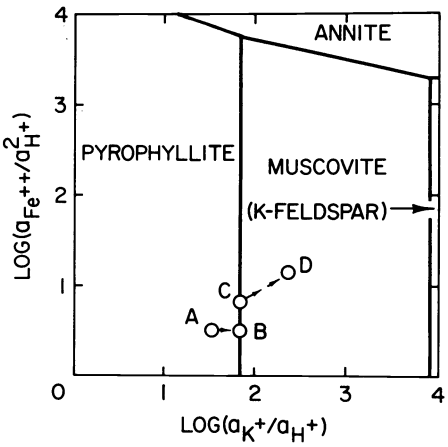

Fig. 24. Logarithmic activity diagram for the system Na_2O–K_2O–Al_2O_3–SiO_2–H_2O–HCl in the presence of quartz for unit activity of H_2O at 300°C and 100 bars. The diagram was generated from equilibrium constants calculated in the manner described in the caption of Fig. 5 (see text). Reaction path ABCD corresponds to the sequence of events depicted in Fig. 21.

remains in that volume by the time the reaction process reaches point D in Figs. 21, 23, and 24. In contrast, if a larger surface area of say 10,000 cm^2 (kg H_2O)$^{-1}$ is specified, the dimensions of the fissure segment become 100 cm long, 50 cm deep, and 1 mm wide. The reaction time represented by ABCD in figures 21, 23, and 24 would then be 2000 seconds and the limiting flow rate would decrease to $\sim$ 160 cm^3 $year^{-1}$, which is nevertheless much faster than that associated with fluid flow in metasomatic processes (Refs. 40 and 41).

The observations and computer experiments summarized above indicate that rates of hydrothermal reaction among minerals and aqueous solutions that are far from equilibrium are essentially instantaneous in the context of geologic time. Taking account of advection and rates of heat and mass transfer by diffusion in aqueous solutions (Ref. 41), it follows that large perturbations from quasistatic states must be ephemeral in geochemical processes. As solution pH increases and the chemical affinities of the reactions decrease, the rates of reaction decrease dramatically as the reactions approach a quasistatic state, which may persist over long periods of geologic time. Under these circumstances, the rates of reaction are controlled by their chemical affinities. The fact that the results of mass transfer calculations like those described above are generally in close agreement with field observations (e.g., see Refs. 10, 32, 37) suggests that the uncertainties involved are within observational error.

CONCLUDING REMARKS

Although the preceding discussion touches on but a few of the many thermodynamic aspects of geochemistry, there can be little doubt that the multidimensional complexities and intricacies of the thermodynamic behavior of geologic systems at high pressures and temperatures are beginning to be appreciated. However, high-temperature solution chemistry is vastly different from its low-temperature counterpart, and much remains to be learned about the behavior of electrolyte solutions in geochemical processes. This is especially true of hydrothermal fluids that are rich in CO_2, H_2S, CH_4, etc. (Ref. 42). Similarly, standard laboratory techniques of investigating reaction rates cannot be used to simulate those in hydrothermal systems, which (for the most part) are in multiple quasistatic states of reaction progress. As in the case of phase equilibrium studies designed to provide reliable data for thermodynamic calculations, the value of laboratory studies of the dissolution kinetics of minerals lies in the extent to which they afford rate parameters to be used in the "thermodynamic" rate laws like that represented by Eq. (21).

Thermodynamics and geochemistry are destined for a long and rewarding association in all aspects of the geological sciences. We can only hope that the extrapolative techniques that are now an indispensible part of theoretical geochemistry will serve as a temporary but useful guide to experimentalists and those who follow in paving the way toward a deeper understanding of geochemical processes in the Earth.

ACKNOWLEDGMENTS

The research described above was supported by the National Science Foundation (NSF Grants EAR 77-14492 and EAR 81-15859). I am indebted to my graduate students at the University of California, Berkeley, who cheerfully contributed time and assistance in carrying out the calculations reported in this paper. I am especially grateful in this regard to William M. Murphy, John C. Tanger, IV, Barbara Ransom, and David Sassani. Thanks are also due Joan Bossart, Joachim Hampel, Mike Salas, and Ingrid Chesnut for technical assistance. The manucript benefited from constructive reviews by Peter Lichtner, William M. Murphy, John C. Tanger, IV, Dimitri Sverjensky, and Eric Oelkers, who made many helpful suggestions for improvement.

REFERENCES

1. Benson, S.W., *Thermochemical Kinetics*, Wiley, New York, 223 pp. (1968).
2. Helgeson, H.C., and Kirkham, D.H., *Am. J. Sci., 274*, 1089-1198 (1974).
3. Helgeson, H.C., Delany, J.M., Nesbitt, H.W., and Bird, D.K., *Am. J. Sci., 278-A*, 1-229 (1978).
4. Helgeson, H.C., *Am. J. Sci., 282*, 1143-1149 (1982).
5. Helgeson, H.C., *Am. J. Sci.*, (in press) (1984).
6. Maier, C.G., and Kelley, K.K., *Am. Chem. Soc. J., 54*, 3243-3246 (1932).
7. Helgeson, H.C., Kirkham, D.H., and Flowers, G.C., *Am. J. Sci., 281*, 1249-1493 (1981).
8. Tanger, J.C. IV, and Helgeson, H.C., Revised equations of state for calculating the standard molal thermodynamic properties of aqueous species in hydrothermal systems at pressures and temperatures to 5 kb and 1000°C, submitted for presentation at the 1984 Annual Meeting of the Geological Society of America.
9. Jackson, K.J., and Helgeson, H.C., Submitted to *Econ. Geol.* (1984).
10 Helgeson, H.C., *50th Anniv. Symposia: Mineralogy and Petrology of the Upper Mantle, Sulfides, Mineralogy and Geochemistry of Non-Marine Evaporites*, Min. Soc. Am. Spec. Pub. 3, 155-186 (1970).
11. Lichtner, P.C., and Helgeson, H.C., *Geol. Soc. Am. Abs. with Programs, 14*, 546 (1982).
12. Bird, D., and Helgeson, H.C., *Am. J. Sci., 281*, 576-614 (1981).
13. Frisch, C., and Helgeson, H.C., *Am. J. Sci., 284*, 121-185 (1984).
14. McKenzie, W.F., and Helgeson, H.C. Submitted to *Econ. Geol.* (1984).
15. Pitzer, K.S., *Proc. Natl. Acad. Sci., USA, 80*, 4575-4576 (1983).
16. Kirkwood, J.G., *J. Chem. Phys., 7*, 911-919 (1939).
17. Haar, L., Gallagher, J., and Kell, G., *Contributions to the 9th Int. Conf. Properties of Steam*, Inst. Phys. Sci. and Tech., Univ. Maryland, 1-14 (1979).
18. Tuttle, O.F., and Bowen, N.L., *Geol. Soc. Am. Mem., 74*, (1958).
19. Burnham, C.W. In, *Geochemistry of Hydrothermal Ore Deposits* (ed. H.L. Barnes), 2nd ed., Wiley, New York, 71-136 (1979).
20. Helgeson, H.C., and Kirkham, D.H., *Abs. of Papers*, Am. Chem. Soc., PHYS-53 (1977).
21. Gates, J.A., Wood, R.H., and Quint, J.R., *J. Phys. Chem., 86*, 4948-4951 (1982).
22. Gibbs, J.W., *Connecticut Acad. Trans., 3*, 343-524 (1878).
23. Bruton, C.J., and Helgeson, H.C., *Am. J. Sci., 283-A*, 540-588 (1983).
24. Franck, E.U., *J. Chimie Physique*, 9-17 (1969).
25. Marshall, W.L., *Rev. Pure and Appl. Chem., 18*, 167-186 (1968).
26. Seward, T.M., In, *Chemistry and Geochemistry of Solutions at High Temperatures and Pressures,* (eds., D.T. Rickard and F.E. Wickman), Pergamon, Oxford, 113-132 (1981).
27. Helgeson, H.C., and Kirkham, D.H., *Am. J. Sci., 276*, 97-240 (1976).
28. Helgeson, H.C., *Am. J. Sci., 267*, 729-804 (1969).
29. Helgeson, H.C., In, *Chemistry and Geochemistry of Solutions at High Temperatures and Pressures,* (eds., D.T. Rickard and F.E. Wickman), Pergamon, Oxford, 133-178 (1981).
30. Bowers, T.S., Jackson, K.J., and Helgeson, H.C., Springer-Verlag, Freiburg (1984).
31. Aagaard, P., and Helgeson, H.C., *Am. J. Sci., 282*, 238-285 (1982).
32. Helgeson, H.C., and Murphy, W.M., *Math. Geol., 15*, 109-130 (1983).
33. Helgeson, H.C., Murphy, W.M., and Aagaard, P., *Geochim. Cosmochim. Acta*, in press (1984).
34. Murphy, W.M., and Helgeson, H.C., Kinetics of transient and steady-state hydrolysis of rock-forming silicates, submitted for presentation at the 1984 Annual Meeting of the Geological Society of America.
35. DeDonder, Th., Leçons de Thermodynamique et de Chimie-Physique. Paris, Gauthier-Villars (1920).
36. Wolery, T.J., Lawrence Livermore Laboratory Pub. *URCL-52658* (1979).
37. Helgeson, H.C., In, *Geochemistry of Hydrothermal Ore Deposits* (ed. H.L. Barnes), Wiley, New York, 568-610 (1979).
38. Rimstidt, J.D., and Barnes, H.L., *Geochim. Cosmochim. Acta, 44*, 1683-1699 (1980).
39. Helgeson, H.C., and Aagaard, P., *Am. J. Sci.*, in press (1984).
40. Walther, J.V., and Orville, P.M., *Contrib. Min. Petrol., 79*, 251-257 (1982).
41. Walther, J.V., and Wood, B.J., Submitted to *Contrib. Min. Petrol.*, (1984).
42. Bowers, T.S., and Helgeson, H.C., *Geochim. Cosmochim. Acta, 47*, 1247-1275 (1983).
43. Helgeson, H.C., *Am. J. Sci., 266*, pp. 129-166 (1968).
44. Franck, E.U., *Angew. Chemie., 73*, 309-322 (1961).
45. Wright, J.M., Lindsay, W.T., and Druga, T.R., Washington, D.C., U.S. Atomic Energy Comm., WAPD-TM-204 (1961).
46. Pearson, D., Copeland, C.S., and Benson, S.W., *Am. Chem.Soc. J., 85*, 1044-1047 (1963).
47. Quist, A.S., and Marshall, W.L., *J. Phys. Chem., 72*, 684-703 (1968).
48. Waldbaum, D.R., and Thompson, J.B., Jr., *Am. Mineral., 54*, 1274-1298 (1969).